ADVANCED FUNCTIONAL MATERIALS
www.afm-journal.de

Functionalized Graphene Superlattice as a Single-Sheet Solar Cell

*Huashan Li, David A. Strubbe, and Jeffrey C. Grossman**

In-plane heterostructure engineering provides unique opportunities to control device properties. Here, a single-sheet solar cell made of a graphene sheet functionalized into 1D channels is explored. Compared to vertical heterostructure architectures based on 2D materials, the single-sheet solar cell shows potential for improved robustness against defects, enhancement of polaron dissociation, extra freedom for functionalization, and coverage of the entire solar spectrum. The partition width, device length, and functionalizations can be tuned independently to optimize the key optoelectronic properties for photovoltaic performance.

1. Introduction

During the past several years, the emerging class of 2D materials has provided desirable electronic and optical properties that would otherwise have been impossible to achieve in the bulk phases.[1] Recently, there has been great interest in lateral heterojunctions based on 2D materials after their successful synthesis with atomic-scale precision,[2–5] which provides an unprecedented opportunity for device design. For example, conductor-insulator lateral heterojunctions between graphene and hexagonal boron nitride (hBN) have been successfully fabricated via scalable processes,[2,6,7] which show promise in atomically thin integrated circuitry[2] and split closed-loop resonators.[7] The idea has been recently extended to lateral junctions in single-layer MoS2 with different phases[3] or dopings,[8] and between WS2 and MoS2,[4] demonstrating the possibility of generating intrinsic in-plane p–n junctions.[4] From a theoretical perspective, there have been a number of works that attempt to understand and optimize the electronic, optical, and thermal properties of in-plane 2D heterostructures.[9,10]

Within the category of in-plane heterostructure engineering, the potential for a single-sheet solar cell is especially attractive, since photovoltaic (PV) device performance requires controlling competing and correlated physical properties. 2D materials are utilized in bulk heterojunction solar cells,[11–15] not as absorbers, but rather to take advantage of the delocalized nature of the wavefunction in the 2D material to improve carrier mobility[13,15] and attain the appropriate energy level alignment to extract free carriers.[13,14,16] When the heterostructure is formed between a 2D material and the surface of a bulk material,[11,12,17,18] precise control over the workfunction[17,18] and doping level[17] can be achieved, leading to substantial improvements in built-in potential and carrier density. A vertical heterostructure of stacked 2D materials can have a controlled interface without defects, strains, or reconstruction. A sufficiently dense stack may give strong absorption in a thin layer.[19]

Given that all of its components would be regularly arranged and chemically connected to each other, a single-sheet solar cell is expected to provide the most control over flux of particles and energy compared to the existing architectures made of 2D materials. Functionalized graphene is a promising candidate for such a device, since in addition to the high carrier mobility, large thermal conductivity, and the ability to sustain high densities of electric current, high-quality graphene could be produced by relatively simple and cheap approaches that show promise for large-scale manufacturing.[1,11] Moreover, by advanced solution processing techniques, chemical functionalization has been realized with both covalently bonded[20–24] and physisorbed[17,25,26] molecules, which results in tunable conductivities[17,22,23,25] and openings of bandgaps.[21,23,25,26]

In this work, we explored a prototype architecture for a single-sheet PV device (**Figure 1**a), wherein the active material is a single graphene sheet functionalized into 1D stripes. Employing a combination of ab initio simulations, empirical models, and scaling analyses, we predict this system to possess strong absorption and desirable charge dynamics, among other advantages, compared to vertical architectures. Our results suggest that both the in-plane and vertical heterostructure architectures should be considered for future device optimization.

While the potential applications of heterostructures of 2D materials have been discussed in previous theoretical work, based on the band alignment between transition-metal dichalcogenides in lateral heterostructures,[10] the concept of a single sheet solar cell has not been proposed to our knowledge. Specifically, a full view of the potential for device operation (including multiple relevant properties computed simultaneously) is still lacking and yet would provide beneficial guidance for experimental efforts aimed at creating and optimizing functional devices. Further, much of the work thus far on in-plane heterostructures has focused on tuning average sheet properties; in contrast, here we explore a single-sheet photovoltaic device that

Dr. H. Li, Dr. D. A. Strubbe, Prof. J. C. Grossman
Department of Materials Science and Engineering
Massachusetts Institute of Technology
Cambridge, MA 02139, USA
E-mail: jcg@mit.edu

DOI: 10.1002/adfm.201501906

ADVANCED FUNCTIONAL MATERIALS
www.afm-journal.de

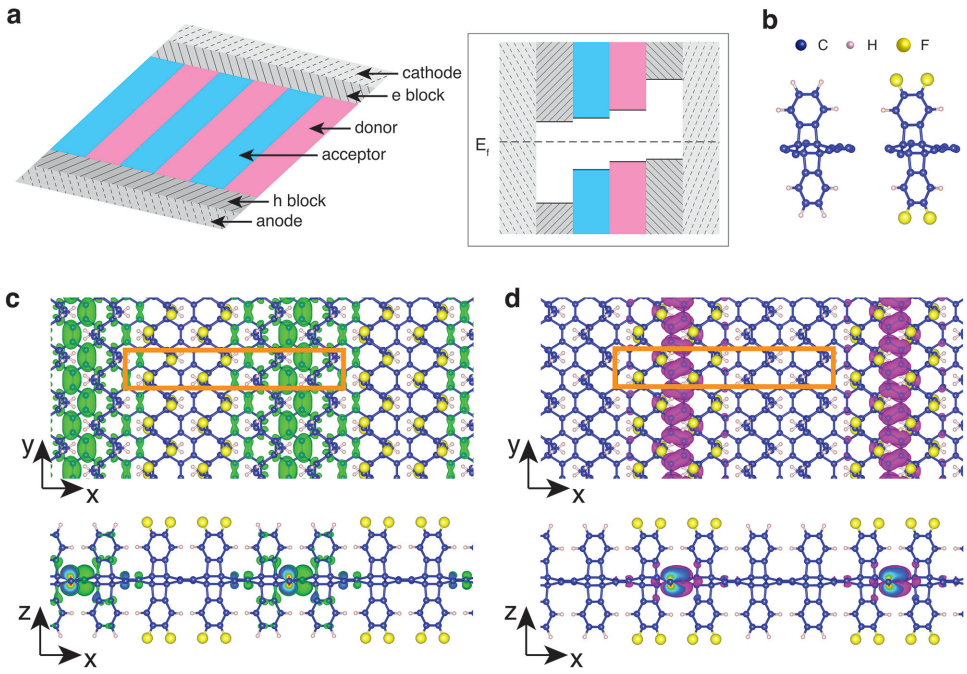

Figure 1. Design of a single-sheet solar cell. a) Generic single-sheet architecture based on a type-II heterojunction in a solar cell device, with required energy-level alignments for efficient operation. b) Structures of benzyne and 3,4-difluobenzyne ligands used to functionalize donor and acceptor regions respectively. Top and side views of c) valence band maximum (VBM) wavefunction in green and d) conduction band minimum (CBM) wavefunction in magenta. The unit cell is highlighted by the orange rectangle.

exploits interactions at the interfaces of the heterostructure, and consider the possibilities for controlling the highly correlated optoelectronic processes.

One possible architecture for a single-sheet solar cell is illustrated schematically in Figure 1a, wherein the active material is an array of aligned nanoribbons. All regions are chemically bonded to their neighbors, but made of different materials or functionalized by different ligands or dopants. With energy alignments as shown, excitons generated in either the donor or the acceptor could dissociate at the type-II interface, followed by carrier diffusion within the 1D domains. By investigating such a system in detail, we find that the single-sheet device shows advantages compared to the vertical heterojunction architecture in four important aspects: 1) robustness against defects may be enhanced because the periodic barriers hinder the carriers from getting trapped by mid-gap states as long as the activation energy is much higher than thermal fluctuations (while a similar mechanism could occur in vertical heterojunctions, the effect is weaker as the isolated domains are much larger); 2) additional freedom for surface functionalization is available given that the overlap between donor and acceptor wavefunctions localized on the sheet may be largely unaffected by the attached ligands, addressing the challenge of maintaining sufficient charge separation in vertical heterojunctions due to the large distance between functionalized sheets; 3) the polaron pair (charge-transfer state) dissociation probability may increase due to weakened Coulomb binding with larger in-sheet donor-acceptor separation compared to that in stacked Van der Waals layers; and 4) the single-sheet device may serve as a building block for stacked tandem solar cells to match the entire solar spectrum, exploiting the fact that the optical gap can be tuned continuously by modifying the functionalization and the width of each partition.

2. Results and Discussion

In order to probe in detail these four potential advantages, we considered a prototype system of a single graphene sheet functionalized by benzyne and 3,4-difluorobenzyne ligands (Figure 1b). These particular ligands are chosen because recent experiments suggest that they can be added to graphene by solution processing,[20] and the strong coupling between the ligand and the substrate allows us to modify the local energy levels via selection of the chemical end groups. The ligands are arranged in the lowest-energy structure reported in previous calculations.[27]

Our electronic-structure calculations show that a type-II energy level alignment is formed between the donor and acceptor regions, with the electron and hole localized in separated areas within the single-sheet (Figure 1c,d). These localized states appear to be quite robust; for example, we observe the same degree of localization independent of the width of the 1D domains, and their wavefunction distribution is insensitive to irregularities at the domain interface (Section C, Supporting Information). In spite of the large binding energy (1.24 and 1.21 eV for donor and acceptor respectively from GW corrections together with a solution to the Bethe–Salpeter equation (BSE)) of excitons localized in each domain, charge separation is still energetically favorable with a driving force of

DOI: 10.1002/adfm.201501906

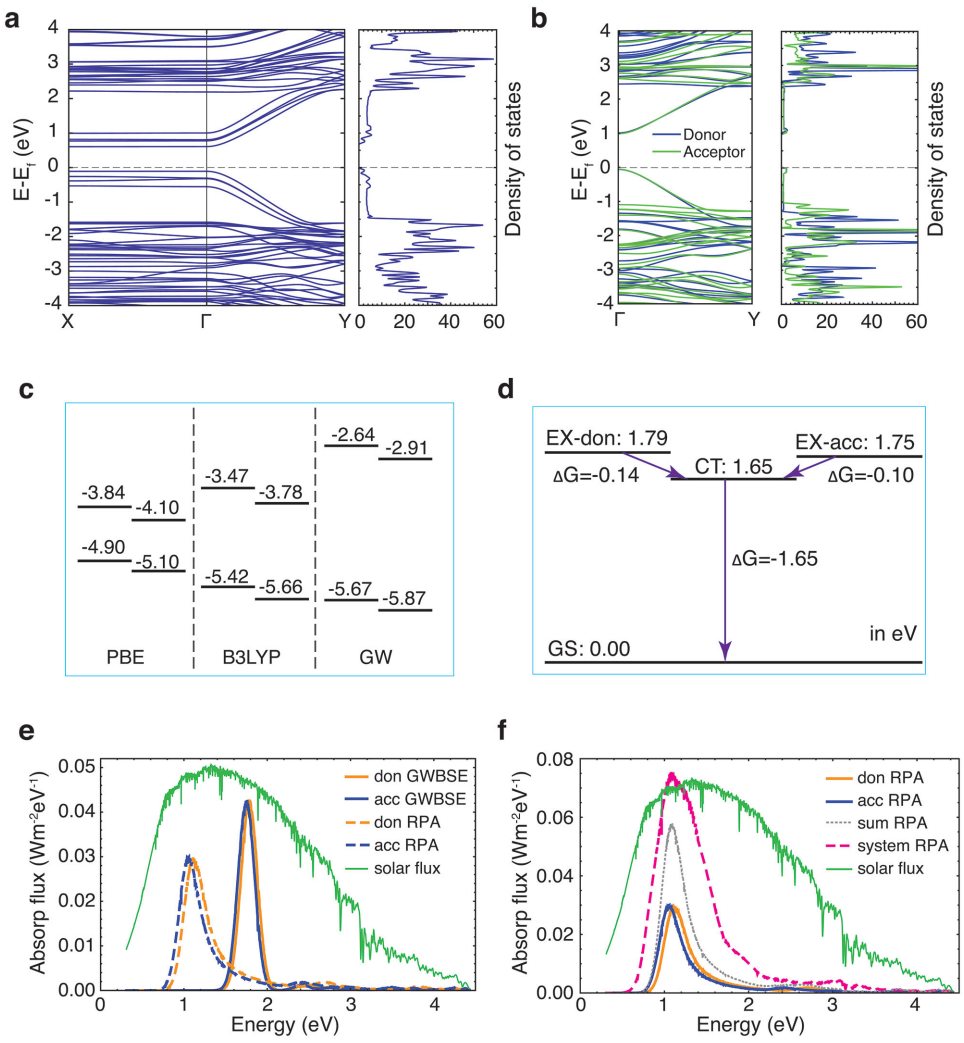

Figure 2. Electronic and optical properties of the prototype system. Band structure and density of states of a) entire passivated graphene sheet, b) donor/acceptor GNR calculated by standard density functional theory (DFT) with PBE functional. The *k*-points shown are Γ = (0, 0, 0), X = (1/2, 0, 0), Y = (0, 1/2, 0). c) Energy-level alignment between donor and acceptor regions calculated by three approaches: both interface potential offset and VBM/CBM obtained from DFT with the GGA-PBE functional; both interface potential offset and VBM/CBM from DFT with the B3LYP hybrid functional; the interface potential offset obtained by DFT with the PBE functional while the quasiparticle corrections were computed by the GW method. (Vacuum level is zero.) d) Energy levels of ground state (GS), local exciton state on the donor (EX-don), local exciton state on the acceptor (EX-acc), and charge transfer state (CT). Both the energy of these many body states and the driving forces (ΔG) for the charge separation and recombination processes are shown in units of eV. e) Absorption spectra of donor (don) and acceptor (acc) GNRs obtained by the DFT random phase approximation (RPA) and GW-BSE approach. f) Absorption spectra of donor, acceptor, their sum, and the full graphene sheet (system) computed by the RPA method. The solar flux is presented in arbitrary units.

0.14/0.10 eV from donor/acceptor domain (**Figure 2**c,d), due to the strong Coulomb stabilization effect between the electron–hole pair in the charge-transfer (CT) state (1.12 eV from integration of the Coulomb interaction between VBM and CBM wavefunction) within this weak screening ($E \approx 1$) system.[28]

The density of states (DOS) and the bandstructure (Figure 2a,b) indicate that while the change from sp^2 to sp^3 hybridization resulting from chemical functionalization opens a band gap in the graphene sheet, no extra bands are introduced by the ligands near the VBM/CBM as their gaps far exceed that of graphene. Nevertheless, mid-gap states could appear in the presence of hydrogen chemisorption and vacancy defects regardless of their positions (Section D, Supporting Information); fortunately, the possible deleterious effects from such states are minimized by the partition of the single sheet into domains. For example, in our prototype system, since the VBM and CBM offsets between the donor and acceptor (0.20 and 0.26 eV respectively) far exceed the thermal energy k_BT (0.024 eV), carriers are unlikely to decay to defect states localized in other 1D domains of the same type via over-the-barrier hopping. Tunneling is also unlikely to occur due to the weak coupling between 1D domains of the same type across the other domains.

As revealed from the flat band structure in the x-direction (perpendicular to the axis of the 1D domain) and large slope in the y-direction (parallel to the axis of the 1D domain)

Table 1. Comparison of carrier mobility and absorption flux between our prototype system and several widely used PV materials. For bulk materials, the absorption flux corresponds to 1 nm thickness.

Material	μ_e [$cm^2\ V^{-1}\ s^{-1}$]	μ_h [$cm^2\ V^{-1}\ s^{-1}$]	J_{abs} [$mA\ cm^{-2}$]
Prototype system	388	93812	0.5
Graphene	200 000	200 000	2.0[e]
Si	650–1300[a]	48–500[a]	0.1[e]
GaAs	1100–1800[b]	100–130[b]	0.3[e]
P3HT	0.00015[c]	0.0003–0.1[d]	0.2[e]

[a] Experiment;[30] [b] Experiment;[31] [c] Experimen;t[32] [d] Experiment;[32,33] [e] Simulation.[19]

(Figure 2a,b), carrier transport should be restricted to the 1D domains. Our computed electron and hole mobilities are much lower than those in pristine graphene, yet comparable to values for widely used inorganic semiconductors and several orders of magnitude higher than most organic semiconductors (**Table 1**). We note that one drawback of such a system is the unbalanced electron and hole mobility, which may be addressed by tuning the width of the graphene nanoribbon (GNR), as shown in previous studies[29] as well as in our present study in Section E of the Supporting Information.

Our prototype system has a predicted absorption flux about four times smaller than that of pristine graphene (Table 1), although still quite a good absorber of light given a thickness of < 1 nm. Compared to a 1 nm thick film of other typical PV materials, our single-sheet PV device absorbs quite well due to its direct band gap character and strong oscillator strength. This may be further improved by adopting conjugated ligands with smaller optical gaps so that they absorb too. Although beyond the scope of this work, transition metal dichalcogenides (TMDs) may be promising candidate materials for a single-sheet solar cell due to their extraordinarily strong light absorption.[19] We note that the positions of the absorption peaks of the combined system are similar to those of the separated GNR components, but the strengths are increased due to the contributions from interfacial and extended states (Section F, Supporting Information).

Even with the strong absorption and appropriate energy-level alignment we have shown thus far, it remains important to predict the charge dynamics which are critical for extracting free carriers from local excitons. As summarized in **Figure 3**a, the charge separation rates for an exciton initially absorbed in either the donor ($1.90 \times 10^{12}\ s^{-1}$) or the acceptor ($4.09 \times 10^{11}\ s^{-1}$) regime are much larger than their respective photoluminescence (PL, radiative recombination) rates (1.72×10^8 and $1.76 \times 10^8\ s^{-1}$). This indicates that excitons would efficiently dissociate into polaron pairs (electron and hole localized in different domains but still bound to each other), which have a much lower charge recombination rate ($5.71 \times 10^4\ s^{-1}$) than

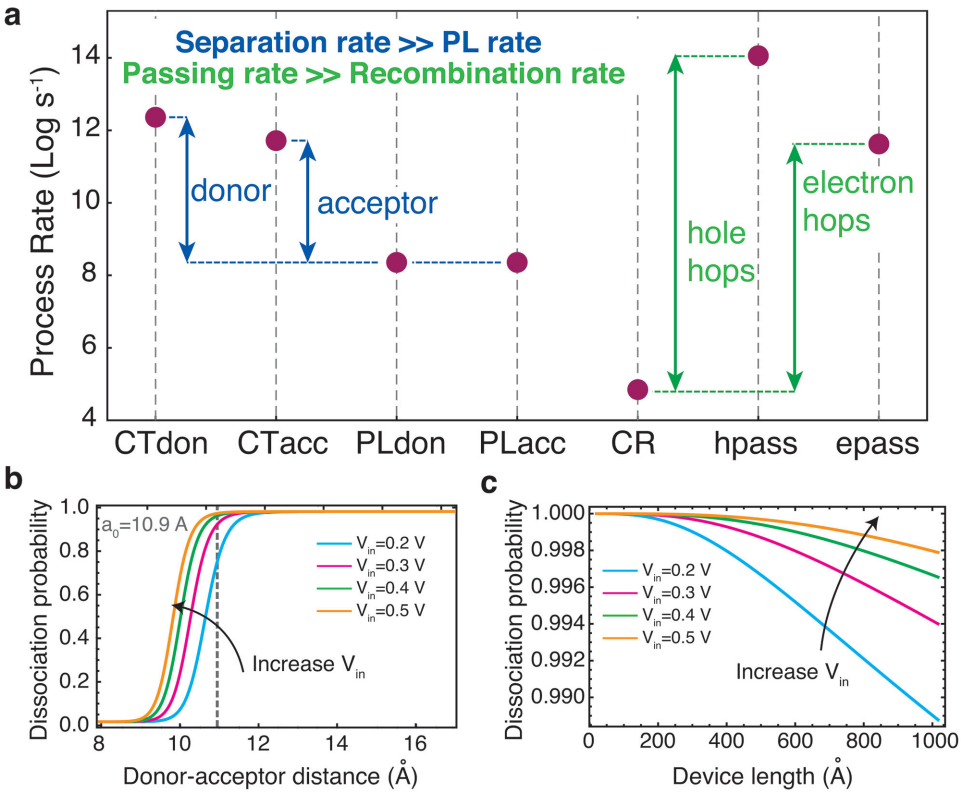

Figure 3. Charge dynamics in light-harvesting processes. a) Charge transfer (CT) from donor and acceptor exciton states, photoluminescence (PL), charge recombination (CR), and electron/hole passing (hpass/epass) rates for the prototype system. Arrows are drawn between competing processes. Change of polaron dissociation probability with respect to b) donor–acceptor distance, c) device length in y-direction and internal voltage drop (V_{in}). The dashed line indicates a_0, which is the center-to-center donor-acceptor distance of the prototype system. The device length is 30 Å in (b), while the donor–acceptor distance is $1.5a_0$ in (c).

Adv. Funct. Mater. **2015**,
DOI: 10.1002/adfm.201501906

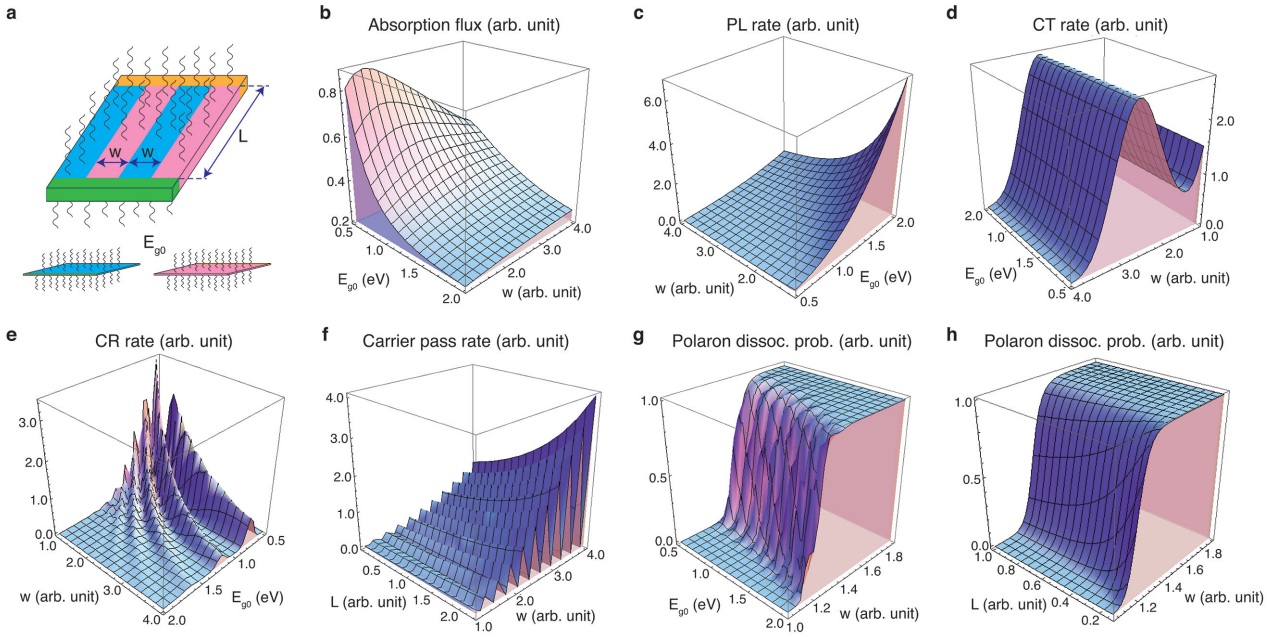

Figure 4. Possibility of optimizing solar cells based on single-sheet device architecture. a) Three control parameters in a single-sheet device. Variation of b) absorption flux c) PL rate, d) CT rate, e) CR rate, f) carrier passing rate, g,h) polaron dissociation probability with respect to the three control parameters. E_{g0} is the optical gap of the donor/acceptor.

the initial excitons, since only nonradiative recombination is now possible. In terms of polaron dissociation, though, the system with relatively small functionalization width (11 Å) is not satisfactory. The dissociation probability in this case reaches 80% only if a strong electric field is built in the device with a very short length of 30 Å (Figure 3b). Fortunately, this may be remedied by weakening the Coulomb interaction with a slightly larger width of the 1D domains, which is illustrated by the estimation of polaron dissociation rates with extrapolation of the binding energy (Figure 3b,c). Once the free carriers are generated, a considerable proportion of them will be able to diffuse to the electrode, as the charge recombination rate (5.71×10^4 s^{-1}) is much lower than the rates (>10^{12} s^{-1}) for electrons/holes to move to the contacts (referred to as carrier passing rates, Figure 3a). Although the individual charge transfer rates could be sensitive to the driving force, reorganization energy and electron coupling, the conclusion that our system is promising for charge extraction is quite robust as the relation between the competing processes does not change over a broad range of configurations (Section H, Supporting Information). Based on the carrier mobility and the charge recombination rate, the diffusion lengths of electron and hole are estimated to be 132 and 2060 μm respectively (Section J, Supporting Information).

While the above analysis illustrates the possible advantages of building a single-sheet PV device, accomplishing these benefits simultaneously is a major challenge due to the correlation between relevant properties. This would be true for any architecture, but an advantage of single-sheet devices is that three parameters can be modified independently: the widths of the partitions (w), the length of the device (L), and the local energy levels of each domain (as a function of ligand type and density, with E_{g0} denoting the optical gap of donor/acceptor) (**Figure 4**a). We have mapped out the influence of these parameters on device performance based on a scaling analysis of GNR systems (Sections I, J, Supporting Information), in which the parameters are chosen to correspond roughly to this prototype system. As summarized in Figure 4b–h, all target functions that characterize the solar cell performance show different dependences on these three structural/chemical controls, which could in turn allow for independent tuning. We note that some of the target functions are more feasible to optimize because of the smooth variation and clear trend. For example, absorption flux could be enhanced either by decreasing E_{g0} to harvest more photons, or by decreasing w to intensify absorption strength. Polaron dissociation probability could be increased either by increasing E_{g0} to reduce charge recombination, or by increasing w to weaken the Coulomb binding effect. Other target functions, such as CT and CR rates, are more challenging to control due to the large fluctuations. Resonant phonon-assisted transitions, with effective barriers of dominant phonon modes close to zero, correlate with the sharp peaks and should be encouraged to improve charge separation while avoided to suppress charge recombination. Even though there is no guarantee that the entire set of six target functions (absorption flux, PL rate, CT rate, CR rate, carrier passing rate, and polaron dissociation probability) can be optimized by controlling only three parameters, the single-sheet device concept provides ample phase space to achieve this goal.

Finally, we note that beyond the active material of the device, which was the focus of this work, further considerations are important to take into account. For example, the electron- and hole-blocking layers will be important for the success of a single-sheet architecture. In principle, these blocking layers could be other parts of the graphene sheet with appropriate

ligands. Such functionalization needs to be designed with appropriate energy-level alignment, high carrier mobility, and small interfacial strain. In addition to blocking layers, high-quality contacts are necessary for efficient charge extraction, which could be realized by the edge-contact geometry that separates the contact metallization from the layer assembly processes.[5] In fact, such 1D electrical contacts have been shown to preserve the ballistic transport in graphene sheets.[5]

3. Conclusion

In summary, we investigated the potential of an in-plane heterostructure solar cell using ab initio simulations. Specifically, a graphene-based single-sheet solar cell is predicted to exhibit desirable characteristics of robustness against defects, efficient polaron-pair dissociation, broad tunability by surface functionalization, and the possibility to modify the optical gap continuously. With such an architecture, the highly correlated optoelectronic properties for photovoltaic performance can be optimized simultaneously via tuning the partition width, device length, and functionalizations independently. Although only the case of a functionalized graphene sheet has been studied in this work, it should be possible to design other devices based on the same underlying principle, which opens opportunities to explore more unique applications of low dimensional materials.

4. Computational Section

We employed DFT with both the B3LYP[34] and PBE[35] functionals within the VASP(v5.3)[36] and Quantum Espresso (v5.0.3) packages[37] to calculate the atomic structure, density of states, bandstructure, charge density, and phonon modes. A one-shot GW approach with the generalized plasmon-pole model[38] was used to account for the quasiparticle corrections, while the Bethe–Salpeter equation (BSE)[39] was applied to calculate the optical absorption with excitonic effects (with a rescaling approach as explained in Section A in the Supporting Information), as implemented in the BerkeleyGW (v1.1) package.[40] The electron coupling was estimated at the Hartree–Fock level[41] with the NWChem (v6.3) package;[42] the carrier mobility was obtained by deformation potential theory within the effective mass approximation;[29] the phonon mode decomposition was computed within the harmonic approximation;[43] and the polaron pair dissociation probability was estimated by the Onsager–Braun model.[44] The PL rates were calculated from Fermi's Golden Rule using BSE eigenstates and the effective mass approximation.[45] The nonradiative charge separation and recombination rates were computed within the phonon-assisted nonadiabatic charge dynamics scenario,[46] with a DOS-weighted average over all possible transitions with positive driving forces.[47] A similar set of approaches has been applied to the Si quantum dot system,[43,48] and similar analyses of the optical spectra and charge dynamics have been carried out on a range of organic,[46,49,50] inorganic,[51] and hybrid interfaces[47] within both natural and artificial systems, which successfully captured qualitative trends observed in experiments.[43,47,49,51] Further details regarding the computational methods employed are provided in Section A of the Supporting Information.

While the DFT calculations are applied to the full system, for the more computationally expensive GW-BSE and charge transfer calculations, isolated GNRs are used to represent the 1D domains, with the interfaces replaced by hydrogen termination. This assumption is justified by the similarity we have observed in the eigenvalues, wavefunctions, bandstructures, density of states, and optical spectra between the GNRs and the combined system, ascribed to the only slight orbital mixing between chemically connected semiconductors (Sections B and G, Supporting Information). We note that in order to make the calculations feasible, we have utilized periodic GNRs and finite fragments for parts of the calculation. We expect this approximation is sufficient for our goal of providing rough estimates for this type of system as opposed to precise predictions.

Supporting Information

Supporting Information is available from the Wiley Online Library or from the author.

Acknowledgements

The authors are grateful to the Eni Energy Frontiers program at MIT for financial support. This research used resources of the National Energy Research Scientific Computing Center, a DOE Office of Science User Facility supported by the Office of Science of the U.S. Department of Energy under Contract No. DE-AC02-05CH11231. This work used the Extreme Science and Engineering Discovery Environment (XSEDE), which was supported by National Science Foundation Grant Number ACI-1053575. The authors thank Dr. Francesca Risplendi for valuable discussions.

Received: May 9, 2015
Revised: June 14, 2015
Published online:

[1] K. S. Novoselov, V. I. Fal'ko, L. Colombo, P. R. Gellert, M. G. Schwab, K. Kim, *Nature* **2012**, *490*, 192.
[2] M. P. Levendorf, C.-J. Kim, L. Brown, P. Y. Huang, R. W. Havener, D. A. Muller, J. Park, *Nature* **2012**, *488*, 627.
[3] R. Kappera, D. Voiry, S. E. Yalcin, B. Branch, G. Gupta, A. D. Mohite, M. Chhowalla, *Nat. Mater.* **2014**, *13*, 1128.
[4] Y. Gong, J. Lin, X. Wang, G. Shi, S. Lei, Z. Lin, X. Zou, G. Ye, R. Vajtai, B. I. Yakobson, H. Terrones, M. Terrones, B. K. Tay, J. Lou, S. T. Pantelides, Z. Liu, W. Zhou, P. M. Ajayan, *Nat. Mater.* **2014**, *13*, 1135.
[5] L. Wang, I. Meric, P. Y. Huang, Q. Gao, Y. Gao, H. Tran, T. Taniguchi, K. Watanabe, L. M. Campos, D. A. Muller, J. Guo, P. Kim, J. Hone, K. L. Shepard, C. R. Dean, *Science* **2013**, *342*, 614.
[6] a) L. Liu, J. Park, D. A. Siegel, K. F. McCarty, K. W. Clark, W. Deng, L. Basile, J. C. Idrobo, A.-P. Li, G. Gu, *Science* **2014**, *343*, 163; b) P. Sutter, Y. Huang, E. Sutter, *Nano Lett.* **2014**, *14*, 4846.
[7] Z. Liu, L. Ma, G. Shi, W. Zhou, Y. Gong, S. Lei, X. Yang, J. Zhang, J. Yu, K. P. Hackenberg, A. Babakhani, J.-C. Idrobo, R. Vajtai, J. Lou, P. M. Ajayan, *Nat. Nanotechnol.* **2013**, *8*, 119.
[8] M. S. Choi, D. Qu, D. Lee, X. Liu, K. Watanabe, T. Taniguchi, W. J. Yoo, *ACS Nano* **2014**, *8*, 9332.

[9] a) J. Y. Kim, J.-H. Lee, J. C. Grossman, *ACS Nano* **2012**, *6*, 9050; b) M. Bernardi, M. Palummo, J. C. Grossman, *Phys. Rev. Lett.* **2012**, *108*, 226805; c) S. Thongrattanasiri, F. H. L. Koppens, F. Javier Garcia de Abajo, *Phys. Rev. Lett.* **2012**, *108*, 047401; d) P. P. Shinde, V. Kumar, *Phys. Rev. B: Condens. Matter* **2011**, *84*, 125401; e) G. Fiori, A. Betti, S. Bruzzone, G. Iannaccone, *ACS Nano* **2012**, *6*, 2642.
[10] J. Kang, S. Tongay, J. Zhou, J. Li, J. Wu, *Appl. Phys. Lett.* **2013**, *102*, 012111.
[11] X. Huang, X. Qi, F. Boey, H. Zhang, *Chem. Soc. Rev.* **2012**, *41*, 666.
[12] Y. Sun, Q. Wu, G. Shi, *Energy Environ. Sci.* **2011**, *4*, 1113.
[13] a) S. W. Tong, N. Mishra, C. L. Su, V. Nalla, W. Wu, W. Ji, J. Zhang, Y. Chan, K. P. Loh, *Adv. Funct. Mater.* **2014**, *24*, 1904; b) C. M. Hill, Y. Zhu, S. Pan, *ACS Nano* **2011**, *5*, 942.
[14] P. Jing, W. Ji, X. Yuan, M. Ikezawa, L. Zhang, H. Li, J. Zhao, Y. Masumoto, *J. Phys. Chem. Lett.* **2013**, *4*, 2919.
[15] a) T. Chen, W. Hu, J. Song, G. H. Guai, C. M. Li, *Adv. Funct. Mater.* **2012**, *22*, 5245; b) G. H. Jun, S. H. Jin, B. Lee, B. H. Kim, W.-S. Chae, S. H. Hong, S. Jeon, *Energy Environ. Sci.* **2013**, *6*, 3000.
[16] a) M. Bernardi, J. Lohrman, P. V. Kumar, A. Kirkeminde, N. Ferralis, J. C. Grossman, S. Ren, *ACS Nano* **2012**, *6*, 8896; b) S. Kaniyankandy, S. Rawalekar, H. N. Ghosh, *J. Phys. Chem. C* **2012**, *116*, 16271.
[17] X. Miao, S. Tongay, M. K. Petterson, K. Berke, A. G. Rinzler, B. R. Appleton, A. F. Hebard, *Nano Lett.* **2012**, *12*, 2745.
[18] a) Y. Lin, X. Li, D. Xie, T. Feng, Y. Chen, R. Song, H. Tian, T. Ren, M. Zhong, K. Wang, H. Zhu, *Energy Environ. Sci.* **2013**, *6*, 108; b) E. Shi, H. Li, L. Yang, L. Zhang, Z. Li, P. Li, Y. Shang, S. Wu, X. Li, J. Wei, K. Wang, H. Zhu, D. Wu, Y. Fang, A. Cao, *Nano Lett.* **2013**, *13*, 1776; c) Y. F. Li, W. Yang, Z. Q. Tu, Z. C. Liu, F. Yang, L. Q. Zhang, R. Hatakeyama, *Appl. Phys. Lett.* **2014**, *104*, 043903.
[19] M. Bernardi, M. Palummo, J. C. Grossman, *Nano Lett.* **2013**, *13*, 3664.
[20] X. Zhong, J. Jin, S. Li, Z. Niu, W. Hu, R. Li, J. Ma, *Chem. Commun.* **2010**, *46*, 7340.
[21] S. Niyogi, E. Bekyarova, M. E. Itkis, H. Zhang, K. Shepperd, J. Hicks, M. Sprinkle, C. Berger, C. N. Lau, W. A. deHeer, E. H. Conrad, R. C. Haddon, *Nano Lett.* **2010**, *10*, 4061.
[22] a) A. Sinitskii, A. Dimiev, D. A. Corley, A. A. Fursina, D. V. Kosynkin, J. M. Tour, *ACS Nano* **2010**, *4*, 1949; b) E. Bekyarova, M. E. Itkis, P. Ramesh, C. Berger, M. Sprinkle, W. A. de Heer, R. C. Haddon, *J. Am. Chem. Soc.* **2009**, *131*, 1336; c) H. He, C. Gao, *Chem. Mater.* **2010**, *22*, 5054.
[23] a) B. Li, L. Zhou, D. Wu, H. Peng, K. Yan, Y. Zhou, Z. Liu, *ACS Nano* **2011**, *5*, 5957; b) C.-J. Shih, Q. H. Wang, Z. Jin, G. L. C. Paulus, D. Blankschtein, P. Jarillo-Herrero, M. S. Strano, *Nano Lett.* **2013**, *13*, 809.
[24] L.-H. Liu, M. M. Lerner, M. Yan, *Nano Lett.* **2010**, *10*, 3754.
[25] W. Zhang, C.-T. Lin, K.-K. Liu, T. Tite, C.-Y. Su, C.-H. Chang, Y.-H. Lee, C.-W. Chu, K.-H. Wei, J.-L. Kuo, L.-J. Li, *ACS Nano* **2011**, *5*, 7517.
[26] J. Park, S. B. Jo, Y.-J. Yu, Y. Kim, J. W. Yang, W. H. Lee, H. H. Kim, B. H. Hong, P. Kim, K. Cho, K. S. Kim, *Adv. Mater.* **2012**, *24*, 407.
[27] P. A. Denis, F. Iribarne, *J. Mater. Chem.* **2012**, *22*, 5470.
[28] K. I. Bolotin, F. Ghahari, M. D. Shulman, H. L. Stormer, P. Kim, *Nature* **2009**, *462*, 196.
[29] M.-Q. Long, L. Tang, D. Wang, L. Wang, Z. Shuai, *J. Am. Chem. Soc.* **2009**, *131*, 17728.
[30] D. M. Caughey, R. E. Thomas, *Proc. IEEE* **1967**, *55*, 2192.
[31] S. M. Sze, J. C. Irvin, *Solid-State Electron.* **1968**, *11*, 599.
[32] S. A. Choulis, Y. Kim, J. Nelson, D. D. C. Bradley, M. Giles, M. Shkunov, I. McCulloch, *Appl. Phys. Lett.* **2004**, *85*, 3890.
[33] R. J. Kline, M. D. McGehee, E. N. Kadnikova, J. S. Liu, J. M. J. Frechet, *Adv. Mater.* **2003**, *15*, 1519.
[34] A. D. Becke, *J. Chem. Phys.* **1993**, *98*, 5648.
[35] J. P. Perdew, K. Burke, M. Ernzerhof, *Phys. Rev. Lett.* **1996**, *77*, 3865.
[36] a) G. Kresse, J. Furthmuller, *Phys. Rev. B: Condens. Matter* **1996**, *54*, 11169; b) P. E. Blochl, *Phys. Rev. B: Condens. Matter* **1994**, *50*, 17953.
[37] P. Giannozzi, S. Baroni, N. Bonini, M. Calandra, R. Car, C. Cavazzoni, D. Ceresoli, G. L. Chiarotti, M. Cococcioni, I. Dabo, A. Dal Corso, S. de Gironcoli, S. Fabris, G. Fratesi, R. Gebauer, U. Gerstmann, C. Gougoussis, A. Kokalj, M. Lazzeri, L. Martin-Samos, N. Marzari, F. Mauri, R. Mazzarello, S. Paolini, A. Pasquarello, L. Paulatto, C. Sbraccia, S. Scandolo, G. Sclauzero, A. P. Seitsonen, A. Smogunov, P. Umari, R. M. Wentzcovitch, *J. Phys. Condens. Matter* **2009**, *21*, 395502.
[38] M. S. Hybertsen, S. G. Louie, *Phys. Rev. B: Condens. Matter* **1986**, *34*, 5390.
[39] M. Rohlfing, S. G. Louie, *Phys. Rev. B: Condens. Matter* **2000**, *62*, 4927.
[40] J. Deslippe, G. Samsonidze, D. A. Strubbe, M. Jain, M. L. Cohen, S. G. Louie, *Comput. Phys. Commun.* **2012**, *183*, 1269.
[41] A. Farazdel, M. Dupuis, E. Clementi, A. Aviram, *J. Am. Chem. Soc.* **1990**, *112*, 4206.
[42] M. Valiev, E. J. Bylaska, N. Govind, K. Kowalski, T. P. Straatsma, H. J. J. Van Dam, D. Wang, J. Nieplocha, E. Apra, T. L. Windus, W. de Jong, *Comput. Phys. Commun.* **2010**, *181*, 1477.
[43] H. Li, Z. Wu, M. T. Lusk, *J. Phys. Chem. C* **2014**, *118*, 46.
[44] C. L. Braun, *J. Chem. Phys.* **1984**, *80*, 4157.
[45] C. D. Spataru, S. Ismail-Beigi, R. B. Capaz, S. G. Louie, *Phys. Rev. Lett.* **2005**, *95*, 247402.
[46] J. Jortner, *J. Chem. Phys.* **1976**, *64*, 4860.
[47] E. Maggio, N. Martsinovich, A. Troisi, *J. Phys. Chem. C* **2012**, *116*, 7638.
[48] H. Li, Z. Wu, T. Zhou, A. Sellinger, M. T. Lusk, *Energy Environ. Sci.* **2014**, *7*, 1023.
[49] a) T. Liu, A. Troisi, *J. Phys. Chem. C* **2011**, *115*, 2406; b) G. Nan, X. Yang, L. Wang, Z. Shuai, Y. Zhao, *Phys. Rev. B: Condens. Matter* **2009**, *79*, 115203.
[50] Y. Yi, V. Coropceanu, J.-L. Bredas, *J. Am. Chem. Soc.* **2009**, *131*, 15777.
[51] I.-H. Chu, M. Radulaski, N. Vukmirovic, H.-P. Cheng, L.-W. Wang, *J. Phys. Chem. C* **2011**, *115*, 21409.